Photon detection at subwavelength scales

Wang, Q.

Chapter 5

An Absorption-Based Superconducting Nanodetector as a Near-Field Optical Probe

We investigate the use of a superconducting nanodetector as a novel near-field probe. In contrast to conventional scanning near-field optical microscopes, the nanodetector absorbs and detects photons in the near field. We show that this absorption-based probe has a higher collection efficiency and investigate the details of the interaction between the nanodetector and the dipole emitter. To this end, we introduce a multipole model to describe the interaction. Calculations of the local density of states show that the nanodetector does not strongly modify the emission rate of a dipole, especially when compared to traditional metal probes[1].

5.1 Introduction

Near-field optical microscopes have been used to probe the fluorescence of a single molecule and the evanescent near field of a large variety of nanophotonic structures [80,81]. Because near-field probes interact with evanescent waves the resolution of these microscopes is not limited by the diffraction limit that holds for propagating waves. Conventional near-field microscopes probe the optical

[1]Q. Wang, and M. J. A. de Dood, Opt. Express **21**, 3682, (2013).

near field with a metal tip [82], a metal particle [83] or a metal coated tip with a subwavelength hole [84]. These probes are positioned in the near field and scanned in the lateral directions. These tips either scatter the light directly into the optical far field, or through a subwavelength aperture connected to an optical fiber where it is detected by a photosensitive detector in the far field.

To attain subwavelength lateral resolution, the size of the aperture or tip should be smaller than the wavelength. This makes near-field probes based on scattering inherently inefficient because light scattering from subwavelength metal particles is an inefficient process. For particles that are much smaller than the wavelength, Rayleigh scattering occurs and the scattering decreases as a^6/λ^4, where a is the dimension of the particle and λ is the wavelength. This low collection efficiency makes near-field studies of quantum optics an extremely challenging task, because detection of weak light with a small collection efficiency (i.e., missing out many photons) introduces noise [46]. Similarly in experiments on single molecules the total number of photons emitted by a molecule is given by the ratio $\tau_{\frac{1}{2}}/\tau_{rad}$, where $\tau_{\frac{1}{2}}$ is the half life of a molecule due to bleaching, and τ_{rad} is the radiative lifetime [85].

Since the absorption of a small particle scales with its volume, i.e., as a^3, an intrinsically much more efficient near-field nanodetector can be constructed. Recently, superconducting nanodetectors have been demonstrated that absorb a single photon and create a measurable electronic pulse for each absorbed photon [14].

In this chapter we consider a detector made of a 4 nm thick NbN film grown on a GaAs substrate, i.e., identical to the square nanodetector reported in Ref. [64]. Photons can be detected only in the constricted area where the current through the detector is close to the critical current of the superconductor at cryogenic temperatures.

5.2 Scattering and absorption by a near-field probe

Conventional scanning near field optical microscopes (SNOMs) can be subdivided into two major types: aperture based SNOMs and scattering type SNOMs [86]. The aperture based SNOMs make use of a subwavelength hole in a metal film or metal-clad fiber tip [87–91]. The transmission through a subwavelength hole in a good conductor is extremely low and is proportional to a^6/λ^4 ($a/\lambda << 1$) [92], where a is the radius of the aperture, and λ is the wavelength of light. Similarly, the scattering type SNOMs make use of light scattering of the sharp end of a metal clad tip to scatter the optical near field directly onto a far-field detector. To estimate the performance of this type of SNOMs the probe is considered to be a sphere [93], and the tip's scattering cross section is then given by Mie theory. As shown in the schematic in

Fig. 5.1, a subwavelength sphere that models the scanning probe, is located above a substrate and is excited at normal incidence light. In this geometry, the tip induces a surface charge in the substrate that can be described by an image dipole at a distance r from the surface [94]. For the sphere one can apply the Rayleigh limit ($a/\lambda << 1$) to calculate the scattering cross section $\sigma = 8\pi|\alpha^{eff}|^2/(3\lambda^4)$ [95], where

$$\alpha_{\parallel}^{eff} = \alpha(1-\beta)/(1-\frac{\alpha\beta}{32\pi r^3}) \quad \text{or} \quad \alpha_{\perp}^{\text{eff}} = \alpha(1+\beta)/(1-\frac{\alpha\beta}{16\pi \mathrm{r}^3}), \qquad (5.1)$$

which represents the effective polarizability of the sphere close to the surface of the substrate. The applied electric field is either parallel or perpendicular to the surface. In Eq. (5.1) the polarizability of a sphere $\alpha = 4\pi a^3(\varepsilon_{sp}-1)/(\varepsilon_{sp}+2)$, $\beta = (\varepsilon_{sb}-1)/(\varepsilon_{sb}+1)$, where ε_{sp} and ε_{sb} are the complex dielectric constants of the spherical particle and the substrate, and a is the radius of the particle [94, 95].

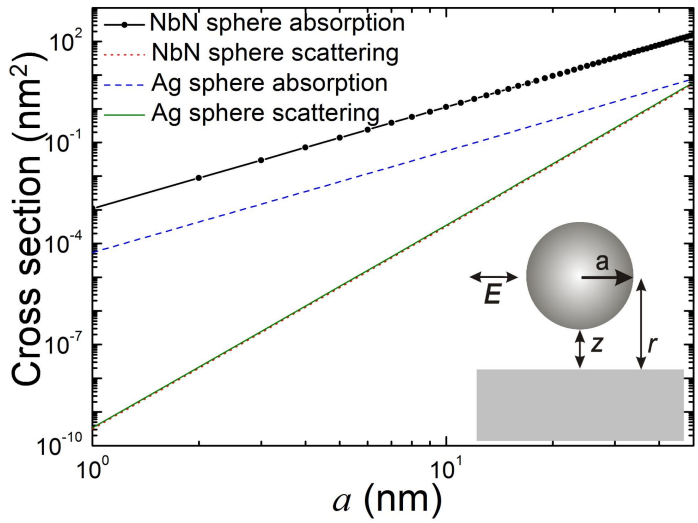

Figure 5.1: Absorption cross section for a NbN sphere close to a GaAs substrate, as compared to a Ag sphere. Calculations are done at $\lambda = 1000$ nm, as a function of sphere radius. The inset shows a sphere with a radius of a at distance $z_0 = 10$ nm from the semi-infinite substrate. The particle is excited by an external electric field E parallel to the interface. In the Rayleigh limit ($a/\lambda \ll 1$), the absorption cross section is much larger than the scattering cross section (Scattering curves for Ag and NbN are overlapped). Because of the larger imaginary part of the dielectric constant of NbN, the absorption cross section of a NbN sphere is approximately 10 times larger than that of a Ag sphere.

Figure 5.1 compares the calculated scattering and absorption cross section for a Ag and a NbN sphere close to a GaAs substrate (refractive index 3.5).

Calculations are shown for light with polarization parallel to the substrate surface with a wavelength of 1000 nm, as a function of the radius a of the sphere. The air gap between the sphere and the substrate is kept constant at $z_0 = 10$ nm as the radius of the sphere is varied. In these calculations we assume a dielectric constant of $\varepsilon_{sp} = -45.6 + 2.9i$ for the Ag sphere [96] and $\varepsilon_{sp} = -8.2 + 31.4i$ for NbN [47].

As can be seen in Fig. 5.1, the scattering cross sections of a NbN and a Ag sphere are comparable in the Rayleigh limit. This reflects the fact that both materials provide a large dielectric constant $|\varepsilon|$ and scattering depends on the absolute value of the polarizability. The absorption cross section of a sphere much smaller than the wavelength is proportional to the volume of the particle, and exceeds the scattering cross section by several orders of magnitude. The absorption cross section of a NbN sphere exceeds the absorption cross section of a comparable Ag sphere by more than an order of magnitude for all sizes. For a realistic, 20 nm diameter tip, the absorption of a NbN sphere is 4 orders of magnitude larger than the scattering of either a NbN or a Ag sphere. Additional calculations (not shown) for vertical polarization and for Au or Al metal are very similar to those presented in Fig. 5.1. A SNOM, based on a NbN nanodetector, that would be able to absorb and detect the radiation directly in the optical near field, would thus comprise a great advantage over current SNOM technology.

A real detector that can operate in the optical near field could be based on a thin strip of NbN material that is tapered down to a constriction which forms the active area [64]. Figure 5.2 compares the absorption cross section of a square detector of size $a \times a$ with the absorption of a NbN sphere of radius a. A schematic drawing of the NbN nanodetector is shown in the inset of Fig. 5.2. The absorption of the NbN sphere is calculated using the Rayleigh approximation for small particles, while the results of a square on a substrate, excluding the wire, are based on finite-difference-time-domain (FDTD, FullWave package, RSoft [71]) simulations. The FDTD calculation includes a 3D model of the square NbN detector on a semi-infinite GaAs substrate. The detector is illuminated at normal incidence by a plane wave with the electric field parallel to the GaAs substrate surface. We monitor the power absorption in the detector and the total intensity of the illumination. From this we calculate the absorption cross section of the square detector. As can be seen from the figure, the absorption of the square NbN detector is larger than that of the sphere, even though the geometrical cross section of the sphere (πa^2) is larger than that of the detector (a^2).

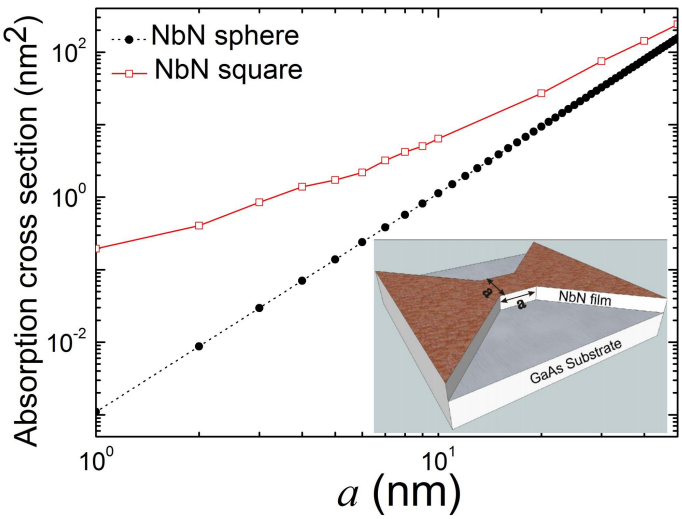

Figure 5.2: Comparison of the absorption cross section for a square and spherical NbN nanodetector as a function of size a at $\lambda = 1000$ nm. Simulations are used to calculate the absorption of a square detector at $\lambda = 1000$ nm. In the optical near field ($a/\lambda \ll 1$), the absorption cross section of a NbN square is larger than that of a sphere. The inset shows a schematic picture of a realistic NbN nanodetector: a 4 nm thick NbN film is grown on a GaAs substrate. A bowtie shape with a nanoscale square constriction serving as the detector active area is patterned in the film.

5.3 Interaction between a NbN detector and a dipole emitter

To evaluate the performance of a SNOM using FDTD we perform simulation of a scanning probe with a light source in the near field. To this end we place a dipole emitter on a GaAs substrate to mimic the single-photon emission from an atom or a quantum dot. Figure 5.3 shows the geometry and the 3D coordinate system used in these simulations. On the surface of a semi-infinite GaAs substrate ($z \leq 0$), a point dipole source is placed at the origin, with its dipole moment along the x-direction, i.e., in the plane of the surface. The square block of NbN represents the nanodetector (50 nm $\times$ 50 nm $\times$ 4 nm constriction), and is situated above the dipole source. Both the detector and the emitter are centered on the z-axis.

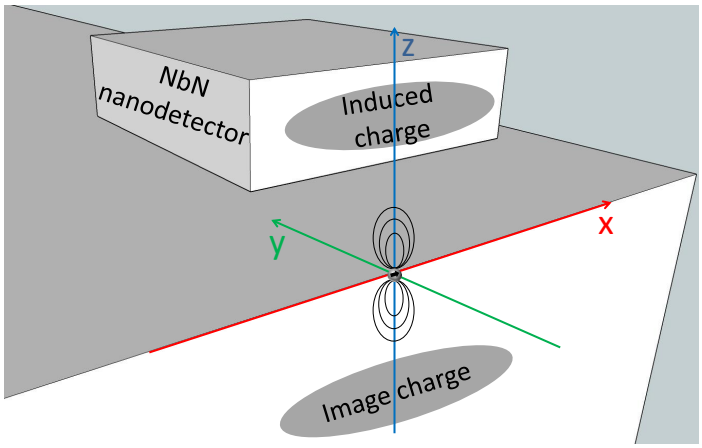

Figure 5.3: Physical model used in FDTD simulations of detector sensitivity and resolution. The NbN nanodetector is located above a dipole emitter (point source) with a dipole moment along x-direction. The emitter ($\lambda = 1000$ nm) is placed on the semi-infinite GaAs substrate. Charge areas are induced inside the nanodetector and in the substrate underneath the emitter.

Several dipole-based models have been put forward to describe the interaction between the tip of the probe in SNOM and the sample [94, 97, 98]. For a scattering SNOM as described in Ref. [94], an analytical dipole model can describe the interaction between the probe tip and a point sample. Within these models, the probe tip is treated as a polarizable sphere that interacts with a dipole source on a substrate.

In our case, when the distance between the nanodetector (probe) and the dipole (sample on substrate) becomes much smaller than the wavelength, a charge area is induced inside the nanodetector by the electric field of the dipole, and the electric potential generated by this charge area can be expressed by a

multipole expansion [79]:

$$\varphi(\vec{R}) = \frac{1}{4\pi\varepsilon_o}[\frac{Q}{R} - \vec{p}\cdot\nabla\frac{1}{R} + \frac{1}{6}\overleftrightarrow{D}\colon\nabla\nabla\frac{1}{R} + \cdots], \tag{5.2}$$

where $\varphi(\vec{R})$ is the potential at the position $\vec{R}$ ($R = \sqrt{x^2+y^2+(z-z_0)^2}$), z_0 is the distance from the dipole source to the detector, ε_o is dielectric constant in vacuum, Q is total induced charge, vector $\vec{p}$ is the dipole moment, and the tensor $\overleftrightarrow{D}$ relates to the quadrupole contribution to the field.

The first term in the brackets of Eq. (5.2) reflects the electric potential generated by the total amount of induced charge Q in the detector. In the detector the amounts of positive and negative induced charge should be equal and this term vanishes.

Within the dipole approximation we only keep the second term in Eq. (5.2), i.e., the dipole moment, and neglect all higher order terms in the multipole expansion. In this chapter, we however, do include the electric field of the induced dipole in the probe (nanodetector) that induces surface charges in the GaAs substrate. This contribution is equivalent to an image dipole in the substrate underneath the dipole source at a distance of $2z_0$ from the probe [94].

The image dipole has a dipole moment $p' = -\beta p$, where $\beta = (\varepsilon_{sb}-1)/(\varepsilon_{sb}+1)$ [94,99], and $\varepsilon_{sb} = 12.25$ is the dielectric constant of the GaAs substrate ($\lambda = 1000$ nm). The total field includes the original dipole field and the contribution from the image dipole fields. The effective polarizability for the probe-sample system (parallel to the substrate) is then given by Eq. (5.1).

With this effective polarizability, the scattering and absorption cross section are calculated in a straightforward way.

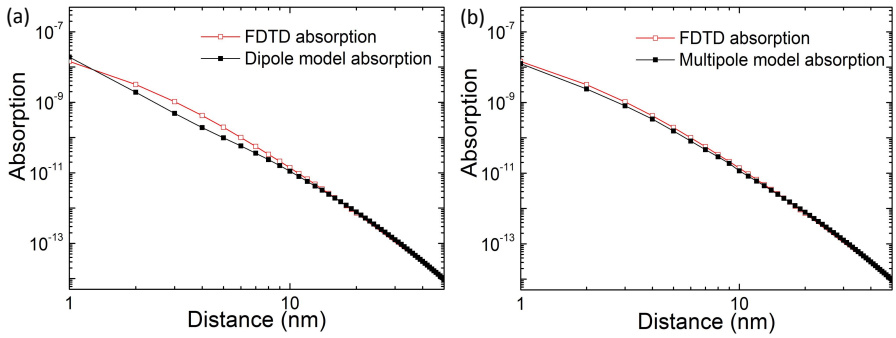

Figure 5.4: Calculated absorption of a point dipole as a function of distance between the nanodetector and the substrate. Calculations are done for a wavelength $\lambda = 1000$ nm with the radiation power of the dipole source fixed at 1 W. The FDTD results are compared with two models: a dipole (a) and a multipole (b) model.

Figure 5.4 shows the absorption in the detector as a function of the distance

between the detector and the dipole. Calculations based on the dipole approximation and complete FDTD are compared. As can be seen in Fig. 5.4(a), a noticeable deviation exists between the absorption calculated by the dipole model and by FDTD for $z < 10$ nm. We explain this deviation by the square shape of the detector instead of a simple sphere for the SNOM tip. In a square detector a more complex image charge distribution exists. This charge distribution cannot be described by an induced dipole only. In order to describe the image charge more accurately, we include a quadrupole moment in the expression given by Eq. (5.2). Figure 5.4(b) shows the absorption in the detector using a multipole expansion (i.e., dipole and quadrupole) and FDTD simulations. Compared to the dipole model above, the multipole model, that includes a quadrupole moment, fits the FDTD curve very well.

To analyze this contribution in a concise way we consider a dipole moment in the x-direction (see Fig. 5.3) that creates an induced dipole in the nanodetector, which is mirrored and points in the $-x$-direction. For the dipole and its induced dipole oriented along the x direction the E_y component of the field in the xz-plane is zero and the electric field is strongly concentrated at the center of the constriction. At this position the field contains only nonzero E_x and E_z components. Hence, we limit our model to the component D_{13} of the tensor $\overleftrightarrow{D}$. The induced quadrupole moment in the detector can then be defined as:

$$D_{13} = \int_V 3xz\rho(x,y,z)dxdydz = \zeta\sqrt{E_x^2 + E_y^2}, \tag{5.3}$$

where we have introduced a tuning parameter ζ that we determine from the comparison of the model with FDTD simulations.

Again, an image charge is induced below the emitter as shown in Fig. 5.3, with $p' = -\beta p$ and $D' = \beta D$ [99], where $\beta = (\varepsilon_{sb} - 1)/(\varepsilon_{sb} + 1)$.

The total electric field $\vec{E}(E_x, E_y, E_z)$ inside the nanodetector contains a contribution from the dipole emitter and the image charge and can be expressed as:

$$\vec{E} = \vec{E}_{emitter} + \vec{E}_{image}, \tag{5.4}$$

which can be solved analytically. To obtain the absorption in the detector we numerically integrate $|\vec{E}|^2$ over the volume of the nanodetector and multiply the result by the imaginary part of the dielectric constant [79]. We neglect phase variations of the electric field in our model, because the near field of a radiant dipole can be treated as a static electric dipole field as long as $kr \ll 1$ (k is the wave vector and r is the distance from the dipole) [79].

At distances larger than 20 nm the interaction between the detector and the dipole emitter is very weak. In this case both the multipole model and FDTD calculations yield almost identical curves with the same tendency that

reflects the rapid decay of the electric field of the dipole source with distance. From the comparison of the multipole model and FDTD calculations we find a value $\zeta = 14.5$ for the tuning parameter in Eq. (5.3). We note that a very small deviation remains in Fig. 5.4(b). We attribute this deviation to the fact that our multipole model does not include the finite size of the detector. In the multipole model we ignore the boundaries of the detector based on the assumption that the quadrupole field decays very strongly towards the edge of the detector.

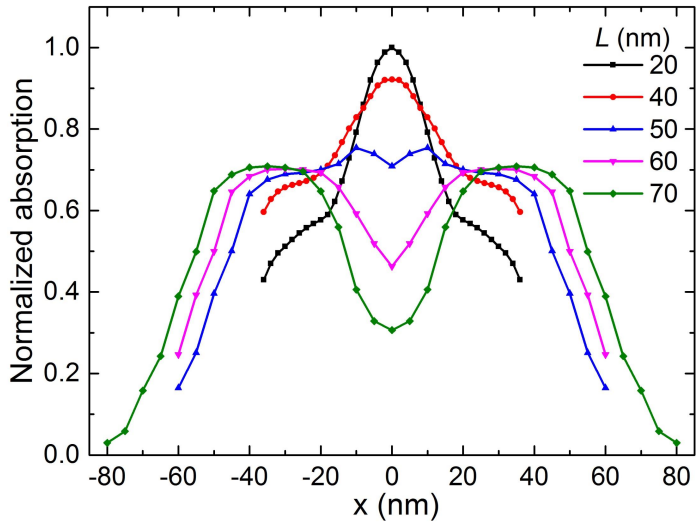

Figure 5.5: The absorption of a 50×50 nm^2 detector when scanning over two dipole sources separated by a distance L. The different curves correspond to different values of L. The two dipoles can be resolved for a separation $L = 60$ nm. The absorption curves are normalized to the maximum for a separation $L = 20$ nm.

For practical applications of the novel, absorption-based, SNOM tip it is important to consider the spatial resolution. To this end, we perform additional FDTD calculations. To estimate the resolution we investigate the response of the detector to two dipole sources separated by a distance L. Figure 5.5 shows the absorption of the detector when scanning the two sources on the substrate surface. The absorption values are normalized to the maximum of the absorption for a separation $L = 20$ nm. The various curves in the figure correspond to different values of the separation L. As can be seen in the figure, two sources at a distance $L = 60$ nm can be resolved, comparable to the transverse size of the detector. The calculations are performed with the detector at a height $z_0 = 10$ nm from substrate. We chose this height to find a compromise between the near-field probe affecting the dipole emitter and a degradation of the resolution that occurs for larger distances of the detector

from the substrate. The most favorable situation is reached for a detector that is as far away as possible, without significantly degrading the resolution. In principle, the spatial resolution can be improved via nanofabrication of smaller detectors by reducing the constriction area of the wire further. However, it is currently unclear how this affects the operation of the detector and what the practical limitations on the active area of the detector are when the resistive region ("hot spot") in the detector is taken into account [64]. The 50 nm constriction considered in this work has been studied experimentally [64] and a spatial resolution of ∼500 nm has been demonstrated.

5.4 The detector's influence on the dipole source/ emitter

In the previous sections, we have discussed the absorption of radiation from an emitter by a nanoscale detector. In this section we will investigate and discuss the influence of the detector on the emitter. It is well-known that near-field probes affect the emitter and can change the decay rate and quantum efficiency of the emitter [100–102]. The change in decay rate is proportional to the local density of states (LDOS) of the system consisting of the near-field probe and the substrate on which the emitter is placed.

In order to estimate the change in emission rate we calculate the LDOS for a simple system consisting of a thin (4 nm thick) NbN film on a semi-infinite GaAs substrate. We are primarily interested in the near-field interaction where the distance between the emitter and the detector is comparable or smaller than the lateral size of the detector. In this near-field regime the change in the decay rate of an emitter close to the detector is expected to be very similar to the change in decay rate induced by an infinite large slab. For the slab configuration, the LDOS can be calculated with relative ease using an analytical expression of the Green's function.

The LDOS $\rho(\vec{R},\omega)$ can be calculated by taking the imaginary part of the trace of the Green's dyadic $\overleftrightarrow{G}\ (\vec{R},\vec{R}',\omega)$ of the system [103]. This quantity is evaluated at the position $\vec{R}=\vec{R}'$, where $\vec{R}'$ is the location of the emitter with transition frequency ω:

$$\rho_{LDOS}(\vec{R},\omega)=\frac{\omega}{\pi c^2}\mathrm{Im}\{\mathrm{Tr}[\overleftrightarrow{G}\ (\tilde{R},\tilde{R},\omega)]\}. \tag{5.5}$$

We use the Green's dyadic $\overleftrightarrow{G}\ (\vec{R},\vec{R},\omega)$ given by the approach of Ref. [100] that separates the dyadic into a nonscattering part $\overleftrightarrow{G_o}\ (\vec{R},\vec{R},\omega)$ and a scattering part $\overleftrightarrow{G_S}\ (\vec{R},\vec{R},\omega)$. The detailed expressions for these quantities can be found in Ref. [102]. For a planar interface with an emitter at a distance

z from the interface the Green's dyadic at the position of the emitter can be significantly simplified. In cylindrical coordinates we obtain:

$$\overleftrightarrow{G}(z,z,\omega) = \frac{i}{4\pi}\int_0^\infty d\lambda[(c_1' e^{i2h_1 z}+1)\frac{\lambda}{2h_1}\hat{e}_r\hat{e}_r + (\lambda - f_1' e^{i2h_1 z})\frac{h_1}{2k_1^2}\hat{e}_\phi\hat{e}_\phi + (f_1' e^{i2h_1 z}+1)\frac{\lambda^3}{k_1^2 h_1}\hat{e}_z\hat{e}_z], \tag{5.6}$$

where $c_1' = (h_1R_1 - h_2)/(h_1R_1 + h_2)$, $f_1' = (S_1h_1\varepsilon_2 - h_2\varepsilon_1)/(S_1h_1\varepsilon_2 + h_2\varepsilon_1)$, with R_1 and S_1 defined as $R_1 = (h_2 - ih_3\tan\theta)/(h_3 - ih_2\tan\theta)$, and $S_1 = (h_2\varepsilon_3 - ih_3\varepsilon_2\tan\theta)/(h_3\varepsilon_2 - ih_2\varepsilon_3\tan\theta)$. In these expressions, k_j denotes the wave vector in j-th layer, h_j is the vertical component of the wave vector and the phase change in the second (middle) layer is θ. These quantities are given by $k_j^2 = \varepsilon_j(\omega/c)^2$, $h_j^2 = k_j^2 - \lambda^2$ and $\theta = h_2 d_2$ respectively, in which c is the speed of light in vacuum, and ε_j is the dielectric constant of j-th layer, and d_2 is the thickness of the second layer [102].

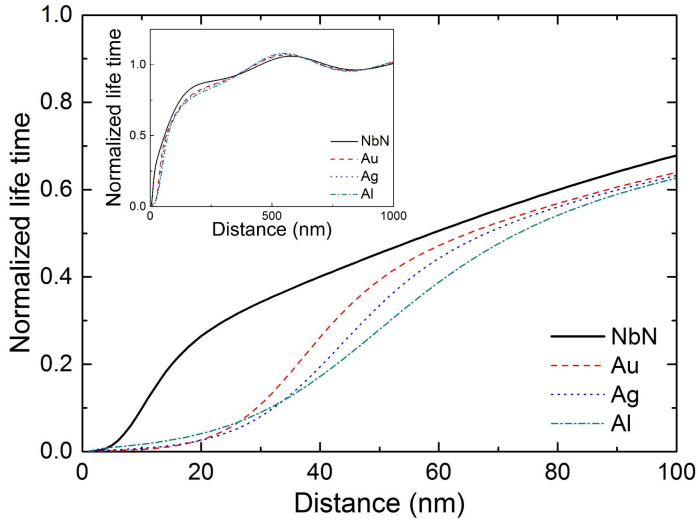

Figure 5.6: Normalized life time of an emitter close to a 4 nm thick metal film as a function of distance from the substrate. Calculation are shown for a NbN, Au, Ag and Al film at $\lambda = 1000$ nm. In the near field (distance < 50 nm), the emitter close to NbN behaves differently from those close to the other three metal films. The inset shows the variations in emitter lifetime for larger distances.

Figure 5.6 compares the normalized life time of an emitter calculated as a function of distance for an emitter close to a 4 nm thick NbN, Au, Ag or Al film. Calculations are shown for a wavelength of 1000 nm. The normalized lifetime is obtained by dividing spontaneous decay rate in free space by the

spontaneous decay rate of the dipole emitter as obtained from the Green's function:

$$\Gamma(z) \propto \omega^2 \mathrm{Im}\{\mathrm{Tr}[G(z,z,\omega)]\}. \tag{5.7}$$

The proportionality constant is divided out by normalization to the life time of the dipole in free space.

The curves in Fig. 5.6 show that the lifetime of the emitter close to the NbN film is much higher for distances below 50 nm compared to the lifetime close to a thin metal film of Au, Ag or Al. This makes a NbN detector a very interesting near-field probe because it has a relatively high detection efficiency while leaving the emission rate of the dipole unaffected. We attribute the relatively weak coupling of the NbN detector to the strong damping in the material that excludes strong energy transfer to the film via surface plasmons. We emphasize that all thin films have comparable reflectivity while only Au, Ag and Al support low-loss surface plasmon modes. This inset shows the calculated normalized life time for distances up to 1000 nm. For larger distances all curves show characteristic oscillations with a periodicity of $\lambda/4$ for an emitter close to a mirror [100]. The modulation of the oscillation around a normalized lifetime of 1.0 is a consequence of self interference between the emitted radiation and radiation reflected by the mirror. These similar oscillations for the different materials are a signature of the fact that reflectivity of the different thin films is comparable.

To further investigate the role of surface plasmons in the near-field interaction for a dipole close to a thin film we calculated the LDOS as a function of angular frequency for different materials. Figure 5.7 shows the calculated LDOS for a 4 nm thick NbN film compared to a 4 nm thick Ag film as a function of frequency. Calculations are shown for a dipole at a constant distance of 5 nm and 10 nm from the metal surface. As can be seen, the calculations for the Ag film show a sharply double peaked structure at angular frequencies close to 3×10^{15} and 7×10^{15} rad/s, while the calculations for NbN show a relatively small maximum around a frequency of 7×10^{15} rad/s.

To calculate these data we use two different modified Drude models [96,104] to describe the dielectric constant of NbN and Ag as a function of frequency:

$$\varepsilon_{_{NbN}}(\omega) = \varepsilon_{_{NbN-high}} - \frac{\varepsilon_{_{NbN-high}}\omega^2_{_{NbN-p}}}{\omega^2 + i\gamma_{_{NbN}}\omega}, \tag{5.8}$$

$$\varepsilon_{_{Ag}}(\omega) = \varepsilon_{_{Ag-high}} - \frac{(\varepsilon_{_{Ag-static}} - \varepsilon_{_{Ag-high}})\omega^2_{_{Ag-p}}}{\omega^2 + i\gamma_{_{Ag}}\omega}, \tag{5.9}$$

where $\omega_{_{NbN-p}} = 5.28 \times 10^{15}$ rad/s and $\omega_{_{Ag-p}} = 1.72 \times 10^{16}$ rad/s are plasma frequencies; $\gamma_{_{NbN}} = 3.77 \times 10^{15}$ rad/s and $\gamma_{_{Ag}} = 2.3 \times 10^{13}$ rad/s are the damping constants of the plasma excitation; $\varepsilon_{_{NbN-high}} = 12.5$ and $\varepsilon_{_{Ag-high}} = 5.45$

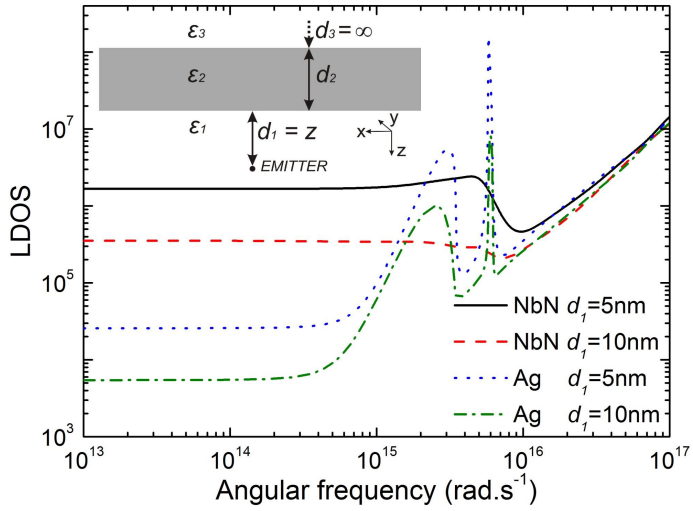

Figure 5.7: Local density of states (LDOS) at the position of the emitter as a function of frequency for different metal substrates. Results are shown for a 4 nm thick NbN film and a 4 nm thick Ag film on a semi-infinite GaAs substrate as shown in the inset. The distance between the emitter and the film is set to 5 nm or 10 nm, which are in the near field of the emitter leading to a strong coupling to surface plasmon modes for the case of a Ag film.

are the relative permittivity in the high frequency limit and $\varepsilon_{Ag-static} = 6.18$ is the relative permittivity in the static limit for Ag.

The data in Fig. 5.7 show that for low angular frequencies below 10^{15} rad/s (wavelength larger than 1800 nm), all curves of the LDOS are very smooth and nearly constant. For frequencies above 10^{16} rad/s (wavelength shorter than 180 nm), all curves approach a LDOS that is proportional to ω^2. In the relevant spectral range between angular frequencies of 10^{15} and 10^{16} rad/s (wavelength range from 180–1800 nm) the calculation for a NbN and a Ag film are markedly different.

The Ag system has two peaks due to the localized surface plasmons. Those sharp fluctuations in LDOS come from the strong energy coupling between the emitter and the Ag film, and this will enhance the energy transfer from the emitter to the Ag that reduces the lifetime of the emitter. These large fluctuations show that the surface plasmon has a profound effect on the emitter and the field that is emitted. In contrast, the LDOS for NbN film shows a much smoother frequency dependence and therefore perturbs the original field much weaker.

5.5 Conclusions

We have introduced a novel, absorption-based, near-field probe based on a NbN nanodetector that absorbs and detects single photons directly in the near field. This nanodetector has a higher detection efficiency compared to conventional scanning near-field optical microscopes because it is based on the physical process of absorption instead of scattering. We calculate an enhancement of 1 to 2 orders by comparing the absorption of a NbN detector with the scattering cross section of a Ag particle using Mie theory in the Rayleigh limit. We introduce a multipole model to describe the near-field interaction between a square NbN detector and a dipole emitter on a GaAs substrate and find that this analytical model fits well with FDTD simulations. From the calculations and FDTD simulations we find that a spatial resolution of $\sim$ 60 nm can be achieved for a detector (50 nm $\times$ 50 nm) at 10 nm distance from the substrate. This resolution is limited by the detector size and may be improved for smaller detectors. Further research on nanodetectors smaller than 50 nm $\times$ 50 nm is needed to find out whether the active area of the detector can be reduced further. A nanodetector close to an emitter also influences the decay rate of that emitter. For good metals with low-loss, large enhancements in the local field can be achieved if the emitter couples to a plasmon mode. For a near-field probe this strong perturbation of the emitter is undesired. We use a Green's function formalism to calculate and compare the change in decay rate for a NbN-nanodetector versus other, commonly used, metals in SNOM tips (Ag, Au and Al). We find that the life time of an emitter that emits at $\lambda = 1000$ nm is only mildly decreased when the emitter is close to a NbN film, while a strong reduction in lifetime occurs for an emitter close to other metals. To explain this difference, we calculate the LDOS at the position of the emitter close to NbN and Ag film as a function of angular frequency of the emitter and show that the surface plasmon on the Ag film causes a strong energy transfer, reducing the life time of the emitter. In contrast, the NbN film has a much weaker coupling to the emitter and does not have a well-developed plasmon mode.

This novel nanodetector could be integrated with a cantilever or a tuning fork as a detection probe. To this end, the superconducting nanodetector should operate in a cryostat ($\sim$ 4 K) to create a near-field scanning optical microscope with high spatial resolution and single-photon and multiphoton sensitivity [64]. This opens new possibilities to explore single emitters, quantum light and optical antenna structures at the nanoscale.